

## Chapter 3

# Experimental Technique

---

This chapter begins with descriptions of how the dHvA measurements were performed, the equipment used and the analysis. Next, a description of the methods and code used to calculate susceptibility is supplied and finally descriptions of the magnetotransport measurements and analysis are detailed.

---

### 3.1 De Haas-van Alphen torque measurement

In this section the measurement of dHvA oscillations by the torque method is described. For decades, the measurement of dHvA oscillations provided the principle method of characterising the Fermiology of a material with only relatively recent competition from techniques such as positron annihilation and ARPES in particular. Whilst ARPES can provide direct maps of Fermi surfaces within the BZ, dHvA has some advantages such as the fact that it <sup>is insensitive</sup> ~~ignores~~ surface effects such as crystal reconstruction, can determine cross-sectional areas with a relatively high resolution and also provides useful secondary measurements such as effective masses of the quasiparticle carriers. Some disadvantages of the technique include the fact that dHvA cannot locate particular cross-sectional orbits within the BZ (thus relies on secondary knowledge such as DFT calculations) and also that the high magnetic fields could potentially affect the Fermi surface, for example by splitting the energy levels. Regardless dHvA continues to be a reliable technique for Fermi surface characterisation.

#### 3.1.1 Experimental apparatus

Much of the experiment apparatus has already been described in great detail by Dr. C. Andrew in her thesis [72] and so only a broad overview and points of difference will be described here.

— You do need your own description though.

### Torque cantilever

A highly sensitive measure of torque is required to pick up the moments experienced by the sample due to the field. For this reason a commercial piezoelectric AFM cantilever, provided by Seiko corps., was repurposed to measure this. The sample was placed onto the ~~topside~~ of the lever above the AFM tip. Previously this would be ~~superglued~~ in place but for these measurements we tried successfully with using vacuum grease which freezes the sample in place at low temperatures. This has the added benefit of still being adjustable and removable when warmed back to room temperature. Moreover, when it comes to rotate the sample in the basal plane, this was possible by nudging the sample gently without having to move the cantilever and risk breaking the lever with the sample permanently affixed. Care should be taken not to get grease on the pivot point of the levers since this will freeze the lever in place at low temperatures. The cantilevers fea-

epoxy

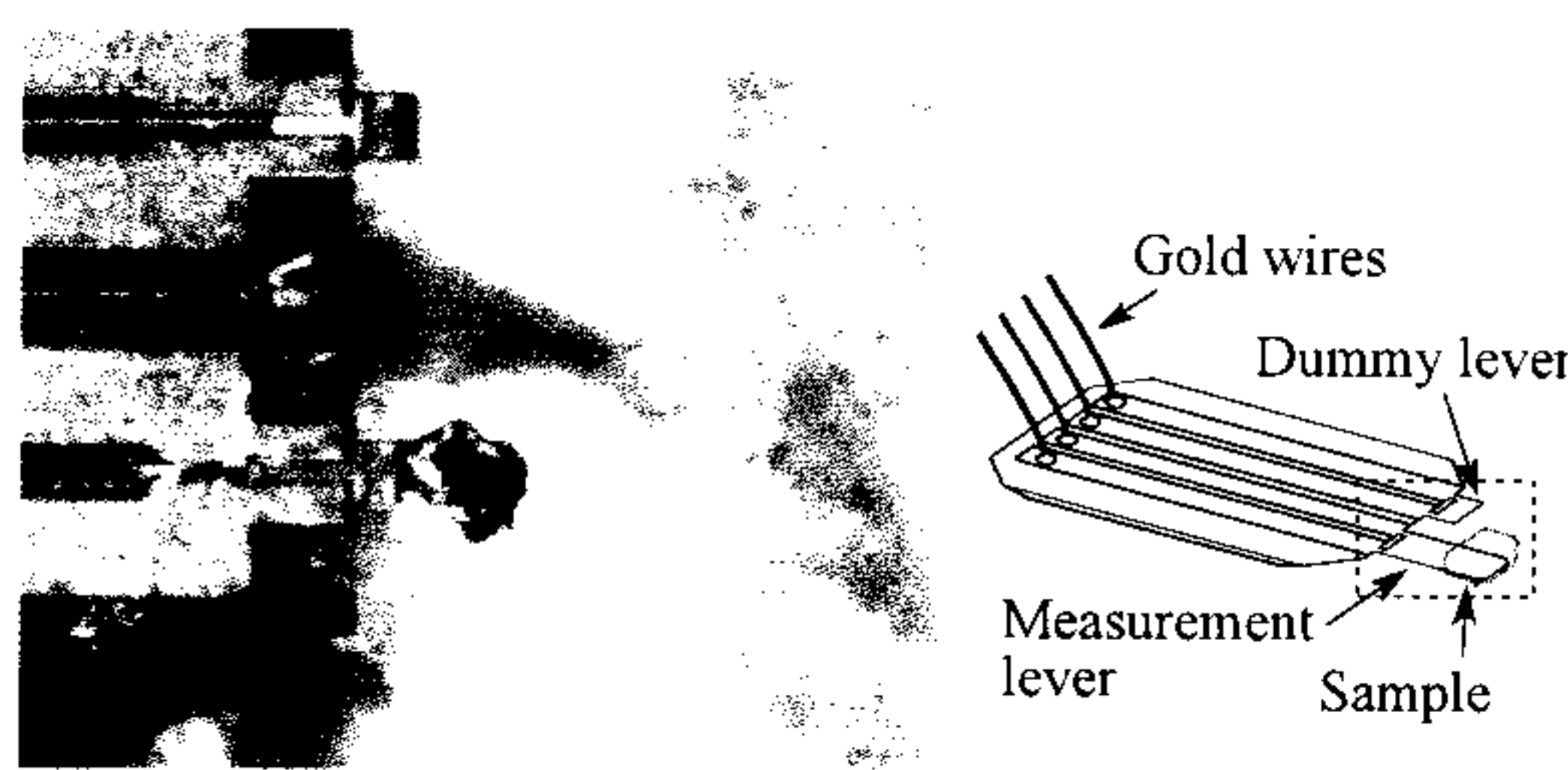


**Figure 3.1.1:** Photo of the  $\text{BaFe}_2\text{P}_2$  sample mounted on the measurement lever along with a schematic showing the full cantilever assembly. N.b. the  $\text{BaFe}_2\text{P}_2$  crystals often cleave along the  $[110]$  plane and so despite the apparent  $45^\circ$  rotation, the sample is aligned such that the lever flexes in the  $[100]$  plane.

ture a second dummy lever alongside the principle lever where the sample was mounted. Instead of measuring the voltage across the principle lever alone, we measure the difference of the voltages between the two levers using a Wheatstone bridge. This enables some degree of correction due to vibrations and fluctuations in measurement current. The circuit is balanced using a variable resistor and is zeroed as best as possible within the noise before each measurement run.

The voltage is supplied and measured using Stanford SR830 lock-in amplifier. The output is first amplified using an EG&G 5113 pre-amplifier with a gain of  $\times 1000$  with a band pass filter which was suitably set for the lock-in

main reason is actually to correct for magnetic resistance.

amplifier excitation frequency.

### Sample stage

The cantilever is mounted onto the sample stage which is a one axis Swedish rotator fabricated entirely from hysol. This is moved by an external stepper motor controlled by a computer.

The angle of the stage in relation to the field is determined by one of two orthogonal pick-up coils mounted on the sample stage. A weak, oscillating magnetic field is generated by a coil which is wound around the sample space such that it is concentric with the main high field coil. The AC coil induces a voltage in these orthogonal pick-up coils on the stage which is proportional to the sine of the angle they are at with respect to the field. The pick-up coil voltage is measured by a second Stanford SR830 lock-in amplifier after passing through a custom amplifier set to  $\times 100$ . The lock-in amplifier also drives the oscillating field after passing a custom built current source. An upper bound on the strength is  $\sim 500$  Gauss, based on a typical measured voltage of 2.2 mV after  $\times 100$  amplification measured across a coil of  $\sim 140$  turns with an average area of  $3.36 \text{ mm}^2$  per loop.

*not really.*

*much too large*

### Yellow Magnet

Measurements of the oscillations were all performed in Bristol on the 'Yellow Magnet' system which was built by Oxford and can nominally operate up to 20 T with use of the lambda plate, an additional cooling system for the magnet coil, although is more typically operated up to 18 T. The bulk of

*20-5T*

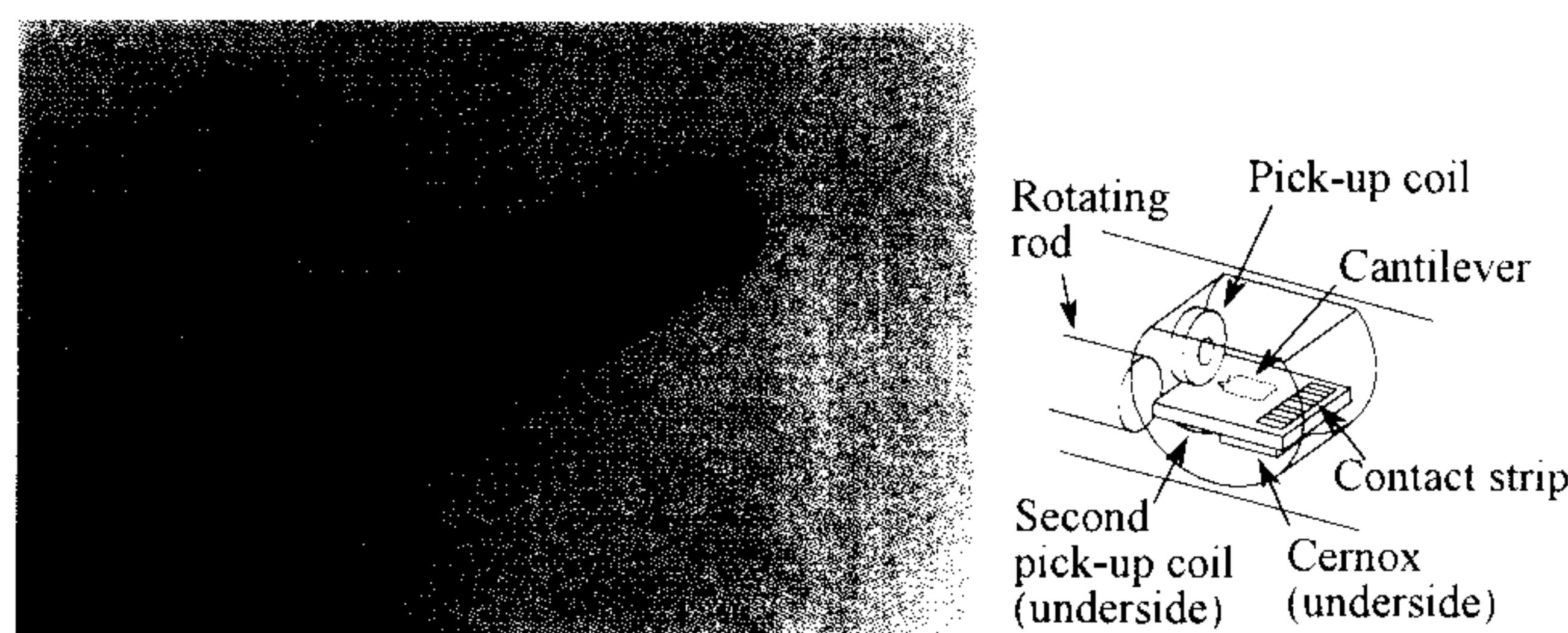


**Figure 3.1.2:** A photo of the Swedish rotator sample stage with cantilever in place and protective cap removed.

the cryostat sits in a bath of  $^4\text{He}$  which takes the temperature down to the



helium boiling point of 4.2 K, and then the sealed sample space is additionally immersed in  $^3\text{He}$  gas in a Heliox system. This system condenses the  $^3\text{He}$  gas at the base of the chamber and pumps on it using a charcoal sorb to lower the sample stage temperature to  $\sim 0.3$  K for several hours before it has to be re condensed. In general measurements are taken at base temperature but higher temperatures can be achieved by heating the charcoal sorb pump thus lowering the pumping rate on the  $^3\text{He}$  bath. This technique allows access to temperatures up to approximately 2.1 K. Temperatures greater than this are possible by heating the sample through an electric heater mounted on the magnet, however it is ~~not possible to accurately control temperature as the field ramps~~ <sup>without set up because we do not</sup> ~~due to magnetoresistance effects in the measurement thermometers.~~ <sup>complications due to</sup> Temperature is monitored at the sample by a Cernox thermometer on the sample stage, and a RuOx thermometer which is mounted in the sample space on the cryostat but is in thermal contact with the tip of the sample stage when the stage is properly seated. Care should be taken that this is the case to ensure good cooling of the sample from the condensed  $^3\text{He}$ . A large mismatch in the temperatures of the Cernox and RuOx thermometers at zero field and base temperature is a good indicator of the sample stage being poorly seated. ~~Further thermometers are situated on the 1 K pot, the sorb and sat on top of the magnet coil although the latter is only monitored when initially cooling the magnet from room temperature. All thermometers and heaters were controlled using two Neocera LTC-21 temperature controllers.~~

Data is collected by a ~~Vigen~~ Windows PC running custom Delphi software which queues measurements and records data only. No analysis is performed in the collection software. Data is saved to text files.

### 3.1.2 Data analysis

#### Angle correction

To perform angle dependent measurements, we need to first of all measure accurately the angle between subsequent measurements and second we need to determine the angle of the field compared to the basal planes of the crystal.

In order to tackle the first problem, the pick-up coils sampling the AC field described earlier are used with the measured voltage begin proportional

for O<sub>2</sub>

not true  
the sealing is  
for pre cooling  
only.

need a diagram

basal

replace  
throughout.

to the sine of the angle between the coil and the AC field. By monitoring this voltage, accurate determination of the angle between the sample platform and the field can be made and therefore the angle between subsequent measurements.

The ~~correct~~ <sup>absolute</sup> angle between the large DC field and the crystal planes in the sample were determined using a post-measurement correction. Since the frequency of the quantum oscillations are field dependent with turning points at the  $B \parallel [001]$  direction for approximately two dimensional samples, an even termed polynomial up to fourth order was fitted to the peaks. From the minima of the fits an angular offset was obtained which gave the final correction to the above coil measurements.

The basel angle was aligned on the cantilever by eye. This was coupled with x-ray diffraction (XRD) measurements which determined how the visual features corresponded to the crystal axes. This leads to an estimated error in basel plane alignment of around 5 % although we found evidence for greater misalignment in one case, detailed in the results.

### Temperature correction

Effective mass measurements on particular extremal orbits rely on accurate temperature determination at all stages of the field sweep. On the Yellow magnet system, temperature from base of  $\sim 0.3$  K to  $\sim 2$  K is controlled by adjusting the He<sup>3</sup> sorbition pump temperature and ~~can be considered to be~~ independent of field effect since the thermometer regulating the sorb temperature is outside of the strong field core. However if we consider figure 3.1.3, it is evident that there are magnetic field effects on the RuOx, which is mounted in the base of the magnet but thermally linked with the sample, and the Cernox thermometer that sits on the sample stage. Readings from both thermometers were taken with field sweeps from zero field up to 18 T at steady temperatures 0.30 K, 0.53 K, 0.64 K, 1.06 K and 1.34 K. By interpolating between this data\*, the two thermometers can be corrected to agree within  $\sim 0.01$  K. This interpolation is however limited to temperatures below approximately 1.45 K as is shown in the figure for readings at around 1.6 K. In these cases, the less reliable method of extrapolating the readings back to zero field using a second order polynomial fit are used as demon-

\*Performed using multiquadric radial basis functions from the Scipy Python library.

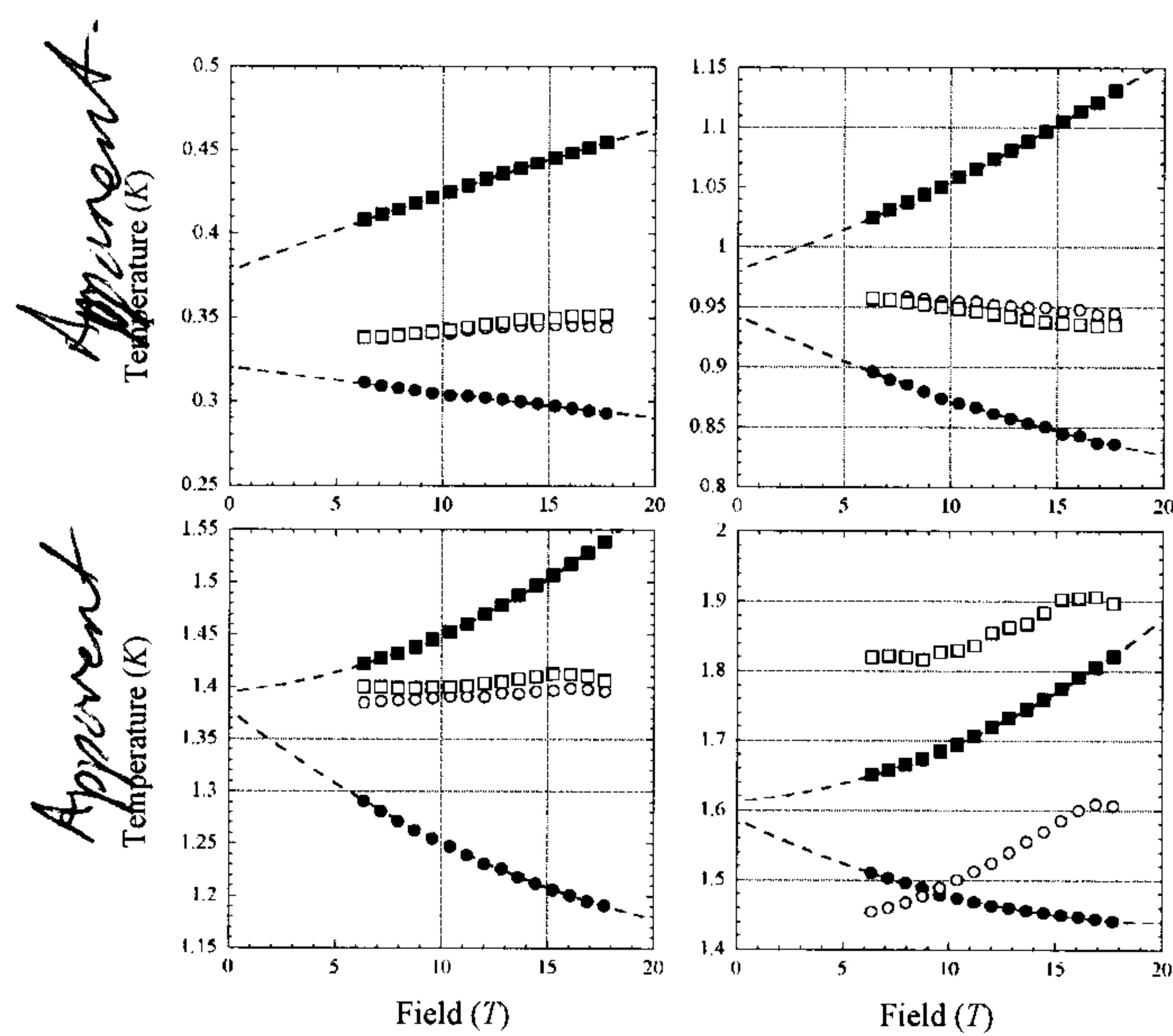


**Figure 3.1.3:** Some example temperature readings (filled symbols) set using the sorbtion pump heater. Also shown are corrections (open symbols) by interpolating to known values. RuOx thermometer is shown as circles, Cernox stage thermometer is shown as squares. Second order polynomial fits to the data are shown as lines extrapolated to zero to get a rough estimate of the zero field temperature value.

strated with the solid lines in figure 3.1.3. In these cases the temperature is taken to be the mean of the two extrapolated values with the differences defining the error.

### Self heating effects

The resistance across the piezo-electric lever is read by driving an AC current through it and reading the voltage across it using the Stanford lock-in amplifier. Larger currents are less prone to noise problems, however too much current results in self heating and subsequently the sample platform and sample could be at a higher temperature than the nearby thermometers suggest. To ensure that this is not the case we measure oscillations at constant temperature with a variety of driving currents. Small currents should not affect oscillation amplitudes, but at some current threshold self heating effects will become apparent and the oscillations are damped as if the entire system was operating at a higher temperature. We then resume measurements using a driving current below this threshold.

Ideally the temperature chosen should be on the steep part of the LK temperature curve (eq. 2.2.13) so that even small changes in temperature manifest in observable changes in the oscillation amplitude.

— state ~~some~~ typical current used and regions where self heating are evident.

### Attenuation due to torque

An extra attenuation occurs due solely to the nature of the torque oscillation measurement. The attenuation factor is given by,

$$A_{\Gamma(\text{gen})} = \frac{1}{F} \frac{dF}{d\theta_{\perp}} V B \quad (3.1.1)$$

where  $V$  is the sample volume and  $\theta_{\perp}$  is angle from the field direction. This can be simplified for a quasi 2d metal to,

$$A_{\Gamma} = |\sin(\theta)| B \quad (3.1.2)$$

where  $\theta$  is the angle from the cylinder axis (usually in the  $c$  direction). This means that at along the cylinder axis there will be no oscillations as  $A_{\Gamma} \rightarrow 0$ .

this is not always an attenuation factor as it can be  $> 1$ .

← what happened to  $V$



### Background removal

Previous standard practice was to remove a background polynomial fitted to the field or inverse field from the raw data before taking the Fast Fourier Transform (FFT). With reference to figure 3.1.4, raw torque data taken over a range of angles\* and a strong  $B^2$  component can be observed as a result of the  $A_{\Gamma}$  term in the LK equation (marked 'B' in the left panel). As shown in the centre and right panels, subtracting a second order polynomial fitted to the *inverse* field leaves a large artificial angle-dependant oscillation in  $1/B$  in the residual which may be misconstrued as a signal from a low frequency Fermi surface orbit, especially since there is an apparent angle dependence – no such peak is seen for the flat curves at 'A' and 'C'. For this reason it is recommended to subtract a second order polynomial fitted to field rather than inverse field for torque measurements.

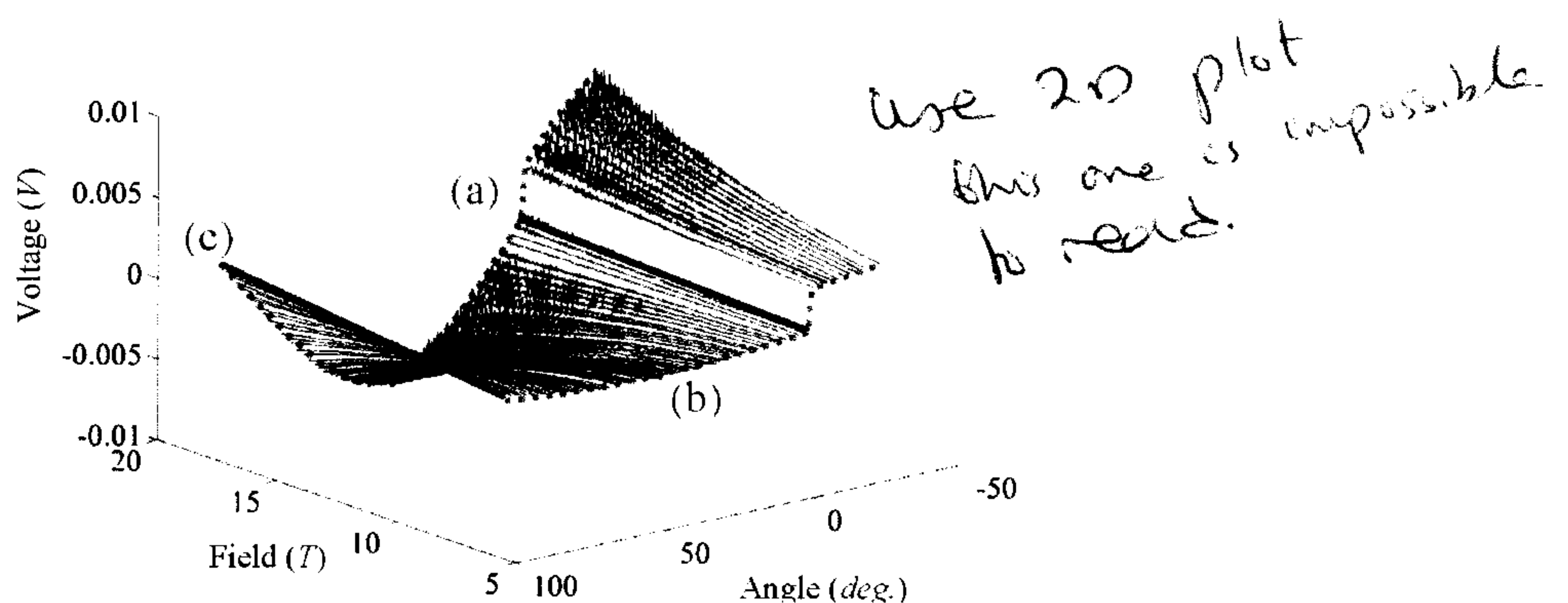


**Figure 3.1.4:** The angle dependence of the raw torque data clearly showing a negative  $B^2$  background at (b) and for  $\theta > 0^\circ$  and a positive  $B^2$  background for  $\theta < 0^\circ$ . The background flattens out at (a),  $\theta = 0^\circ$  and (c),  $\theta = 90^\circ$ .

### 3.1.3 Measuring the spin mass

The only terms in the LK equation that cause the amplitude to drop to zero as a function of angle are the torque term,  $A_{\Gamma}$  which causes a single zero when the field is parallel with the cantilever arm and the spin term  $A_S^\dagger$ . By examining the amplitude as a function of angle it is possible to determine the spin effective mass. A good determination requires more than one spin

\*See section 4.3 for full details

<sup>†</sup>The angle dependence of  $A_S$  comes from variations in the band mass

could also be caused by beating between close frequencies.  
e.g. Tl2201 or MgB2



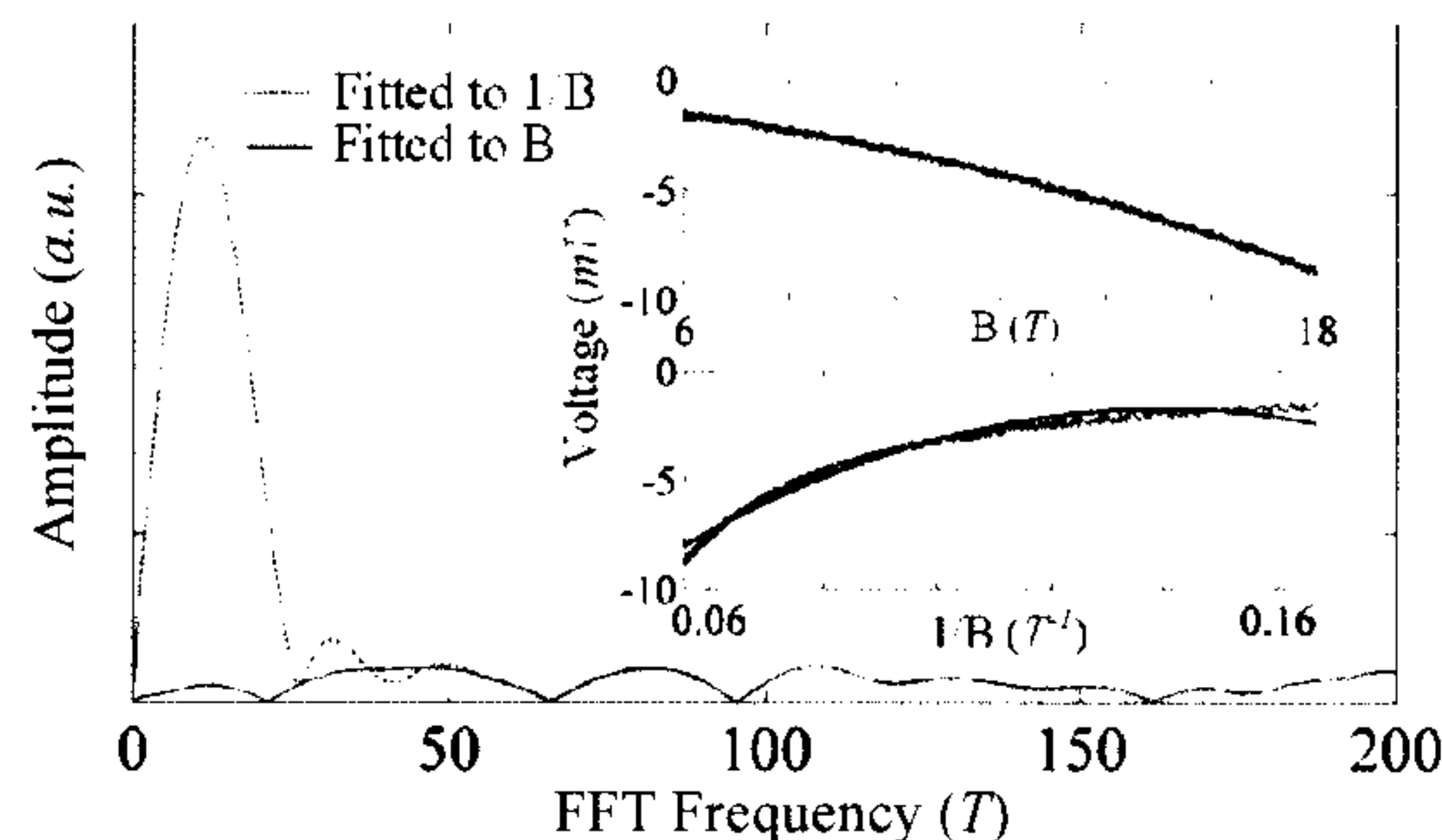


**Figure 3.1.5:** Insets show a 2nd order polynomials fitted to simulated  $B^2$  background with  $\sim 0.5$  mV of noise, similar in scale to that of (b) in figure 3.1.4. Upper inset is fitted to field and lower to inverse field. The main figure shows the resulting FFTs.

zero (i.e. a non torque term zero) to be measured since the oscillatory nature of the  $A_S$  term gives multiple solutions if we only have measured a single zero. We use  $n$  to label each of the zeros from the  $A_S$  oscillations.

In practice the determination is complicated by the fact that if the Landau levels are very well defined, the double peaks due to Zeeman splitting do not overlap and so do not interfere. This manifests as a splitting of amplitudes which do not necessarily drop to zero. In these cases the zeros have to be best determined as being within the region where a noticeable increase in the number of spin split peaks occurs. Moreover, fitting the overall shape requires all of the LK terms to be considered which makes free parameter fitting very difficult to converge. For these reasons, spin mass for this investigation is found from ansatz guesses for the values which are then fitted by inspection. Upper and lower bounds for the estimations are provided.

To the first approximation, the cylindrical approximation is used to describe the band mass in  $A_S$ , however the form of the spin term is relatively sensitive to small deviations and so fits would be much better using a more accurate variation of band mass with angle. Band mass was extracted from DFT results and was performed using Ed's MATLAB code which locates the extremal areas from the corrected BZ energy dispersion at a particular angle. Once located a small shift in energy is applied and the corresponding shift in area is used to determine the band mass using equation ???. A polynomial of appropriate order is then fitted to the curve and used in the fitting routine in place of the band mass. The MATLAB code determines

✓ ok.

I don't think this is correct.

Ed's

the masses with some spread in the values which caused higher order polynomial fits to oscillate at low angles within the noise. To alleviate this, a mean value was determined for each angle.

One final note is that the absolute value of the  $A_S$  term is used to fit the data since we analyse the height of the FFT peaks of the oscillations which are always positive and not the oscillations directly. *← could also look at the phase.*

### 3.1.4 Extracting effective mass from the temperature dependence

Of all the damping terms in the LK equation, only  $A_T$  (eqn. 2.2.13) *is temperature dependent.* ~~and so this is used to determine any kind of temperature dependency.~~ This term also features the thermal effective mass. By measuring oscillations at a fixed angle but with varying temperatures, the effective mass can be determined in a number of ways.

#### Basic LK formula fitting

The simplest technique to extract the thermal effective mass is to extract the amplitude of the oscillations from FFTs of the data at various  $T$  and then perform a least squares fit to eqn. 2.2.13. A particular problem with this approach is that it is not clear what value of  $B$  should be used since the FFTs cover a range of fields. Generally the simplest thing to do is to take the FFTs over a small a range as possible and then take the field to be equal to the averaged inverse field\*.

There are two problems with this approach. First the amplitude tends to decrease with narrowing field range meaning weak oscillations may require larger field intervals. Secondly wider field ranges mean other attenuation factors — which are also functions of  $B$  — affect the amplitude across the field sweep. The primary problem in this case is the Dingle term which has an exponential dependence on  $B$ . Nonetheless, simple LK fits are usually the first port of call and serve as a first approximation to the final result. For this investigation though, since we found some disagreement within the data, we employed a couple of additional techniques described below to overcome this shortcoming.

---

\*That is  $B_{av}^{-1} = \frac{1}{2}(B_{min}^{-1} + B_{max}^{-1})$

*but is not T dependent  
so you need to explain  
why this is a problem.*

**Retrofitting ansatz LK formulae**

One of the primary field-dependant contributions to the oscillation amplitude is the Dingle term scattering (equation 2.2.15) which has an exponential dependence with temperature. The Dingle factor,  $\alpha \neq -\pi p m_0 / e \tau$ , can be determined by fitting a simplified version of the LK equation,

$$\Gamma_{\text{sim}} = A_D(\alpha, B) \sqrt{B} \sin \left( \frac{2\pi F}{B} + \phi \right) \quad (3.1.3)$$

to oscillations which have been band pass filtered to reduce the number of contributions from other extremal orbits and hence the number of necessary fitting parameters. Once we have the Dingle term and also the peak frequency for a particular orbit, simulated oscillations are generated using the same equation but including the temperature term,  $A_T(m_T^*, B)$ , for a range of ansatz effective thermal masses. We then fit this to the LK equation as described in the previous section. The mass that results from the fit is different from the actual effective mass used as the LK fit has been affected by the Dingle term contribution. When we find a simulated oscillation that outputs the same effective thermal mass as the plain LK fit on the actual data we then take the ansatz thermal mass for that matching fit to be the corrected thermal mass.

The filtering used to originally separate out the frequencies is band pass FFT using a Hann window. This is adjusted in size and roll off width according to the peak. Occasionally, the peaks are too close together to effectively filter out individually and so two or three peaks were fitted at a time using a linear combination of the simplified equation above.

The initial fits were filtered using a Delphi program written by Prof. Carrington and fits to find  $\alpha$  were performed in Kaleidagraph. Ansatz fits were found using a binary search technique using a Python script.

**'Microfitting' the LK formula**

A second technique is to filter out the individual orbit frequency by again using an FFT filter and a Hann window, and this time fitting small sections of sine curve ( $\sim 1.5$ – $3$  wavelengths) directly to the filtered torque data. This gives a field dependent value for the amplitude which can then be fitted to the standard  $A_T$  form for many values of  $B$ . The result is a plot of mass

values against  $B$ . Theoretically, these should plateau to give a constant value for the effective thermal mass.

Calculations were performed using a Python script to filter the data, perform the ‘microfits’ and then perform the LK fits. The script was tested using simulated data.

### 3.2 Density Functional Theory

Calculations presented in this thesis were performed using WIEN2k version 07.2 (20th Feb 2007) [73] using LAPW without the local orbitals. Unless specified, non-spin orbit calculations are presented although spin-orbit calculations were checked and did not show significant differences. The GGA according to Perdew-Burke-Ernzerhof [67] was used for the exchange ~~distribution~~. *correlation functional.*

Preprocessing of the WIEN2k data into voxel form as well as the theoretical angle plots were performed using a modified version of MATLAB code written by Dr. E. Yelland. The basis for the code has been thoroughly field tested within the group over a number of years.

### 3.3 Calculating susceptibility

Code to calculate the Lindhard susceptibility was written in MATLAB \* and early versions were tested with free electron cases in 2 and 3 dimensions with results shown in figure 3.3.1. This matches the ~~expected free electron curves~~ *analytical results*.<sup>†</sup> One caveat when dealing with the free electron case is that the energy dispersion is not periodic and as such needs to be truncated at some point in a spherically symmetric way. This truncation affects the final calculation but provided it occurs far enough from the Fermi surface then the difference is minimal. The results shown are for a calculated region that was a sphere of radius 1 with a Fermi surface radius of 0.3. Values for  $\delta(=1e-9)$  and  $\omega(=1e-9)$  are somewhat arbitrary given that the dispersion is simplified with  $\hbar^2/2m = 1$  but are given here for posterity.

The code was adapted to accept pre-generated energy dispersions as calculated with the WIEN2k DFT software and post-processed with Ed’s

\*Full code is found in appendix ??

<sup>†</sup>See, for example, page 126 and Appendix F of reference [61]

this is not experimental technique



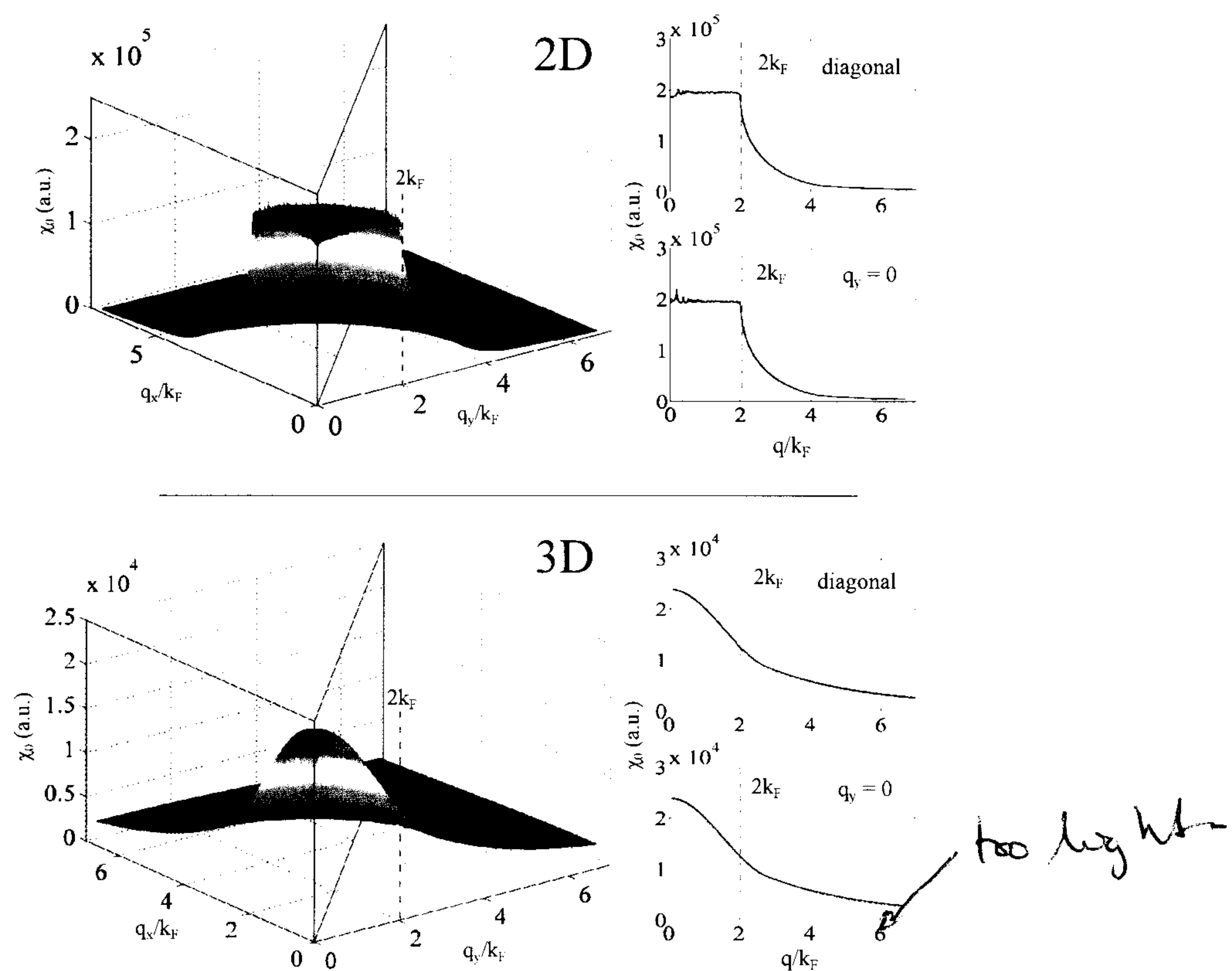


**Figure 3.3.1:** The real part of the Lindhard susceptibility calculations for a free electron model at  $T=0$  K using the MATLAB `calc_x0.m` code. Top panels are for the 2D case over a  $500 \times 500$  point grid, the bottom panels are for the 3D case taken over a  $100 \times 100 \times 100$  point grid. Panels to the right correspond to slices through the surface plots on the left. Calculations in the 3D case are at  $q_z = 0$ .

- can you plot the analytical result on top!?

MATLAB code. In this case, the dispersion is periodic and energies at the scattering vector  $q$  are obtained by simply ‘rolling’ the 3D matrix of energy values. Testing on this adapted code was performed by re-creating WIEN2k calculations on  $\text{LaFeAsO}_{0.1}\text{F}_{0.9}$  performed by Mazin et al. [25] and then comparing our own susceptibility calculations with those in the Mazin paper. A temperature smearing of 1 mRy was quoted which ~~was equated~~<sup>8</sup> ~~using the Boltzman conversion~~ to a temperature of 157.88 K. A similar amount of points ( $55 \times 55 \times 26$ ) was also used.

Figure 3.3.2 show comparisons of  $\text{Re } \chi_0(q, \omega)$  and  $\text{Im } \chi_0(q, \omega)$  with the published results. For these calculations the values of  $\delta = 1\text{e-}4$  and  $\omega = 1\text{e-}6$  were determined to give the closest results from a series of trials\*. The comparison shows that some of the finer structure from the Mazin paper is missing from our own calculations, for example the depression in the real part at the  $\Gamma$  point, however the overall shape is very similar.

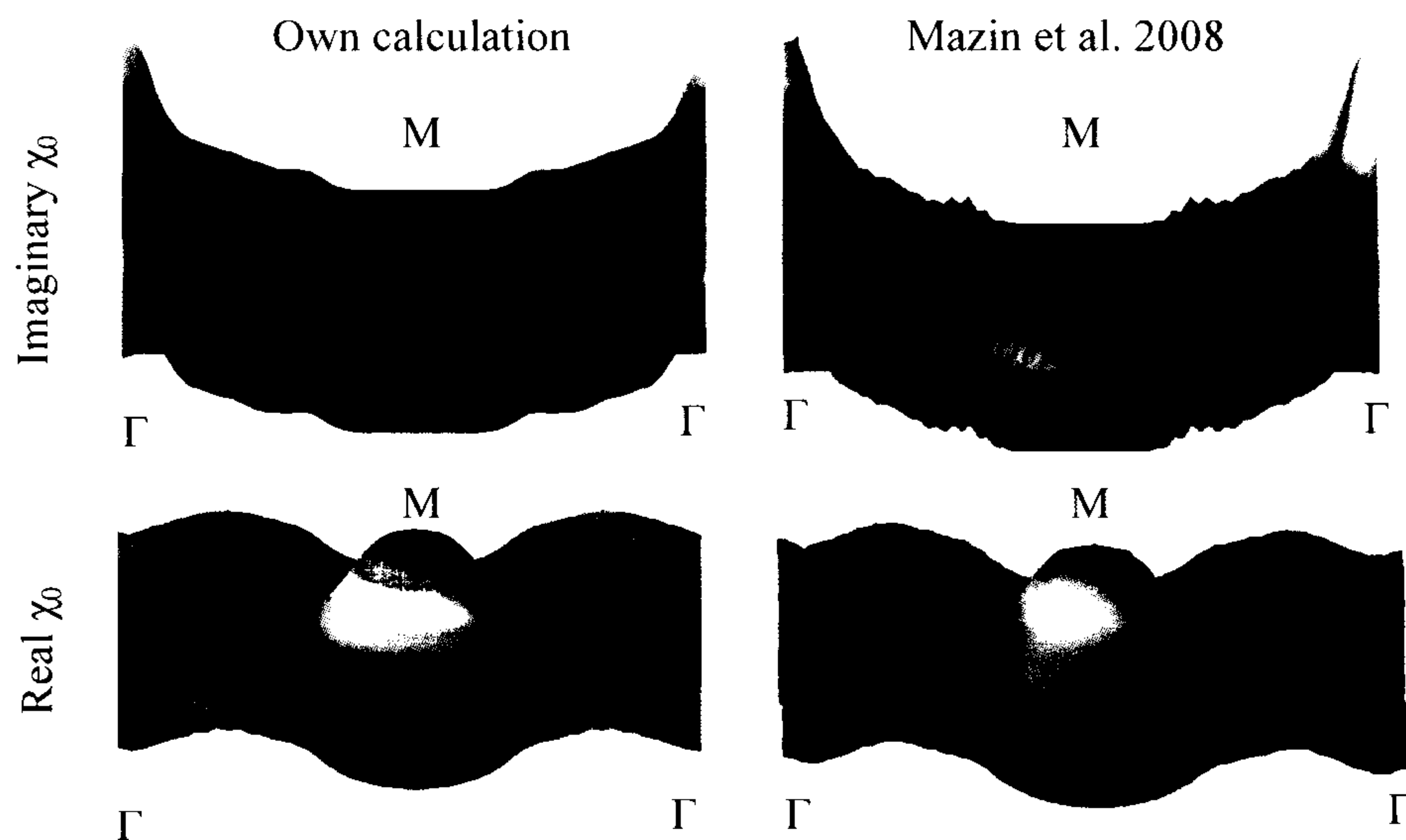


**Figure 3.3.2:** Right hand panels show the real and imaginary parts of Lindhard susceptibility calculations on  $\text{LaFeAsO}_{0.1}\text{F}_{0.9}$  by Mazin et al. for  $q_z = \pi/c$ , right panels show the same calculation performed using our own MATLAB code.

The Lindhard function is very sensitive close to the Fermi surface and finite sampling of the energy data can cause imperfect cancellation in the

\*There is no indication in the paper as to the values of  $\delta$  and  $\omega$  used in their own calculations although we know that they are likely to be of the order of the temperature energy scale (1 mRy) or less.

Show  
Colorbar  
So that meaning  
Colour scale is evident

to details?

calculation — particularly in the imaginary part. Applying a temperature smearing to the function is useful to gloss over the finite element size in the calculation which can cause significant spikes in the results. Figure 3.3.3 shows the smearing at a series of temperatures and that a temperature of 158 K corresponds approximately to a smearing over 2 grid intervals at the Fermi surface. An appropriate choice of temperature depends on the granularity of the model as well as the expected fine detail of the results. The Mazin investigation was into a similar quasi two-dimensional pnictide material that used a comparable number of data points and so we also opted to use 158 K for the temperature smearing.

Smearing also occurs when a finite quasi-particle lifetime,  $\delta$ , is factored in and when the perturbing field is oscillatory with frequency,  $\omega$ . These values are also not known a priori and so we again look to the energy scale of the spacing between grid points close to the Fermi surface for guidance.

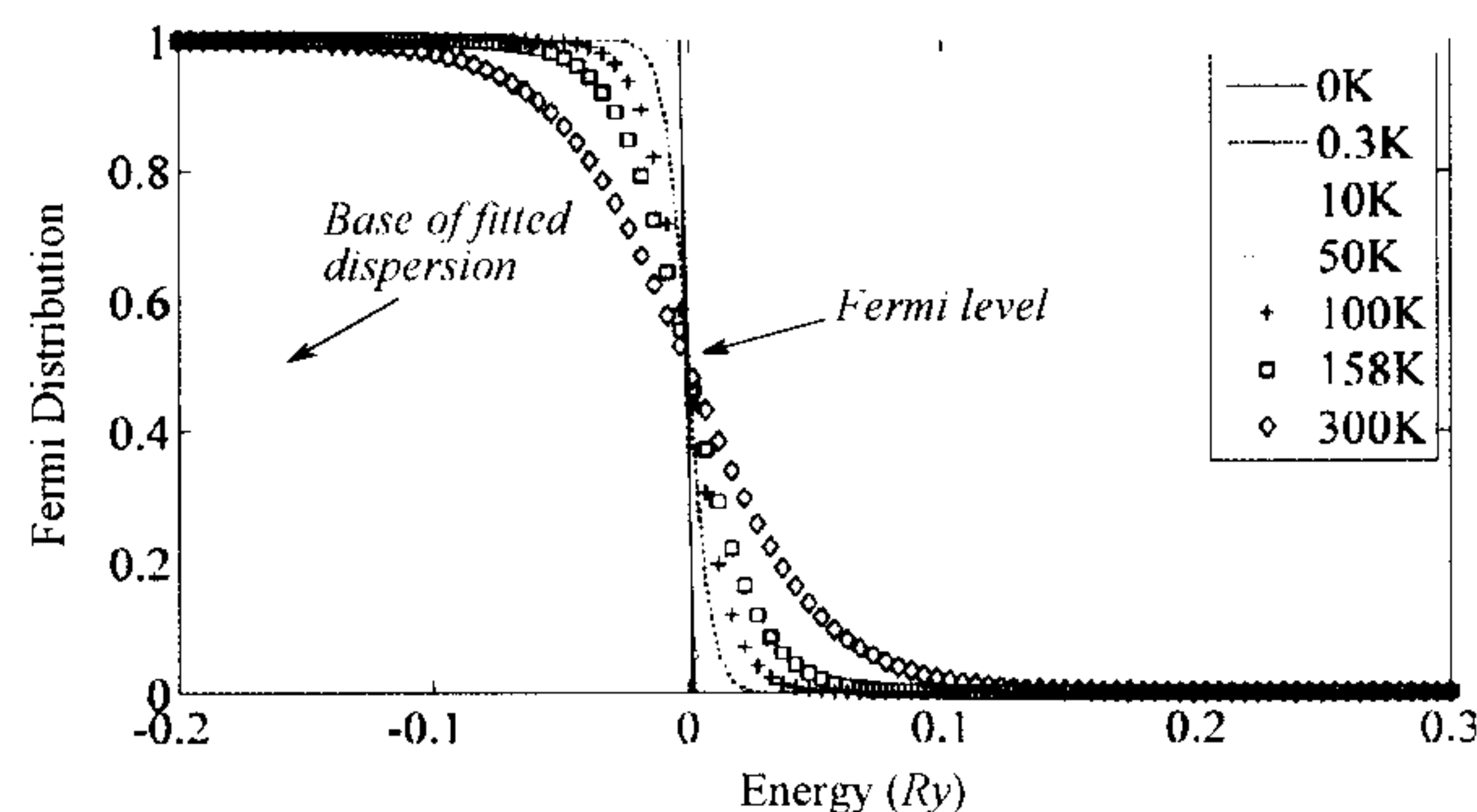


**Figure 3.3.3:** The Fermi distribution plotted at various temperatures. Vertical lines represent typical grid energy spacings for a free electron distribution fitted to a portion of bandstructure for  $\text{LaFeAsO}_{0.9}\text{F}_{0.9}$  which rounds out just below the Fermi surface. We can see that for 158 K, the smearing spans approximately 2 grid intervals at the Fermi energy.

### 3.4 Measuring charge transport

In this section the Hall measurement technique and analysis of the  $\text{BSCO}_{2201}$  samples is described. Transport measurements on superconductors have been performed for over a century now and was the technique by which superconductivity was first discovered. The relative technical simplicity of the measurements makes transport measurements highly appealing considering

the wealth of information that can be extracted from a resistance curve.

The charge transport measurements performed for this thesis took place in Bristol in the Green 'Polo' magnet for low fields and in the LNCMI pulsed field facility in Toulouse for the high field data. Also included is analysis of data taken by <sup>other</sup> group members\* at the HFML in Nijmegen, Netherlands. The overarching six-probe measurement technique is used for all the transport measurements with differences chiefly in measurement geometry and apparatus.

### 3.4.1 Experimental apparatus

#### Six probe technique

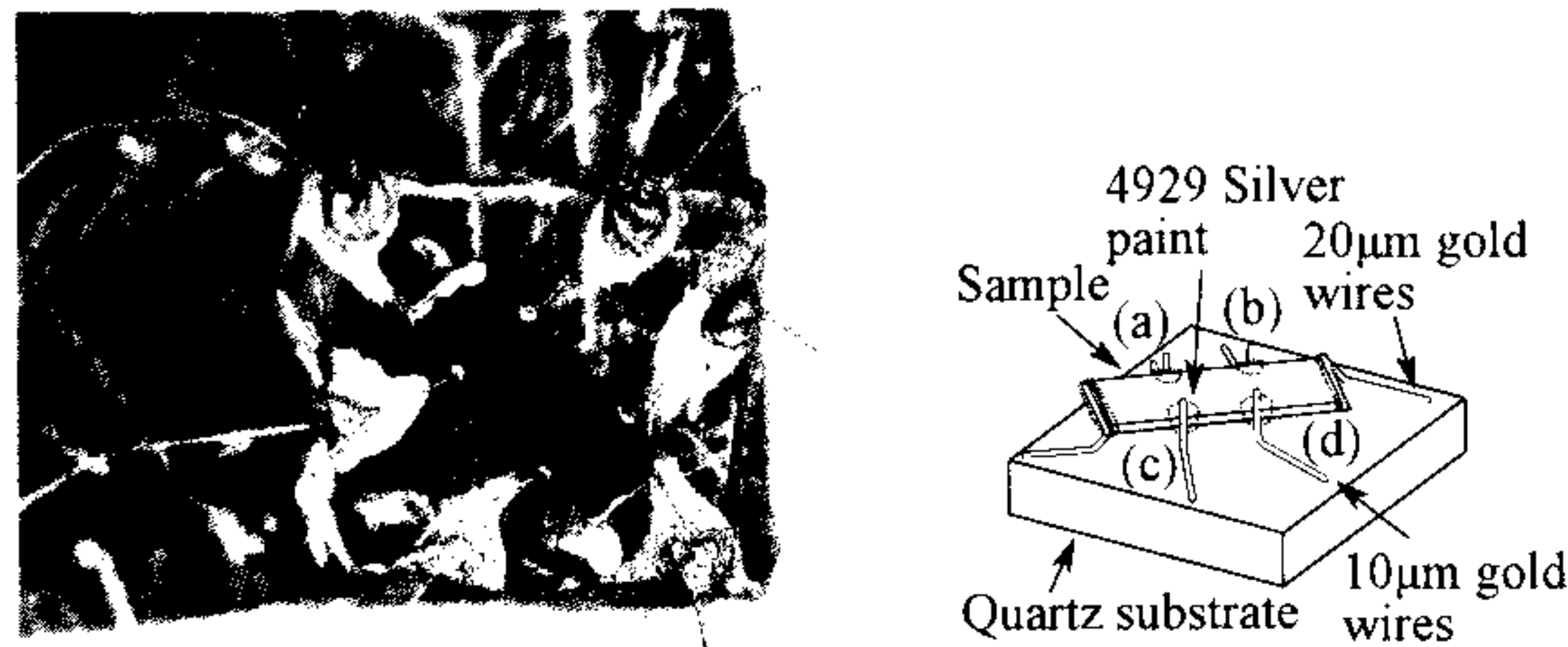
For accurate measurement of voltage, and hence resistance, across a sample, two wires are not sufficient. The wires themselves have a resistance which is comparable or often larger than the resistance of the sample being measured. A solution to this problem is to instead supply the current for the voltage reading via one set of wires, and then take the voltage reading from another set meaning that a minimum of four wires and four contacts on the sample are required. To measure magnetoresistance we require the voltage wires to be placed upstream and downstream of the current; to measure the Hall effect we require the wires to be placed transverse to the current. Moreover it is useful to be able to take two transport measurements ~~at a time~~ so as to get an idea for the homogeneity of the sample and as well to provide some redundancy in case of breakage. Since the BSCO<sub>2201</sub> samples that we studied were to have both measurements, six connection points were placed <sup>on</sup> each sample as shown in figure 3.4.1. The connections were made with 20  $\mu\text{m}$  gold wire for the current and 10  $\mu\text{m}$  gold wire for the voltage leads and attached with DuPont 4929 conductive silver paint which dries at room temperature. As shown in the figure, the sample is raised from the quartz substrate so that when the temperature drops and the wires and sample thermally contract at low temperatures, there is some give so that the ensemble does not pull itself apart. <sup>due to thermal contraction</sup>

With the four voltage legs a variety of configurations can be achieved. Measuring across (a) and (b) is the magnetoresistance configuration, (a) and (c) is the Hall configuration. It is also possible to measure across (a) and

---

\*Dr. X. F. Xu, Dr. P. Rourke and I. Mouzoupoulou





too small.

**Figure 3.4.1:** An example BSCO<sub>2201</sub> crystal mounted on the quartz substrate. Voltage legs are labeled (a), (b), (c) and (d).

(d) and provided the field is reversed from positive to negative, both the Hall and the magnetoresistance across the sample can be extracted.

Because the connections may not be exactly aligned and because the silver paint in practice tends to whet over the edge of the sample, magnetoresistance contributions may be found in the Hall configuration and vice-versa. For this reason it is generally advised to sweep both with a positive field to obtain  $R_{\text{pos}}$  and a negative field to obtain  $R_{\text{neg}}$  where  $R$  is the resistance and separate the two out using the technique described in the analysis section.

Later as the samples has been measured many times and thermal cycling had caused the silver paint to become brittle, it was necessary to attach short,  $\sim 2$  mm, secondary gold wires to each of the contact pads using silver paint and then attach the probe flying leads to the end of these wires. When removing the samples from the probe, this allowed the joins to be immersed in solvent held in the tip of a pair of metal tweezers at a safe distance from the sample ensemble meaning the connection could be dissolved without flexing the contact pads unnecessarily. This was done for the later measurements in the Polo magnet where the minimisation of wire loops was not so important.

#### Polo magnet

The 'Polo' magnet is an ~~Cryogenic~~ <sup>(Cryogenic Ltd)</sup> cryostat containing a ~~Variable~~ <sup>Variable</sup> ~~Temperature~~ <sup>Temperature</sup> ~~Insert~~ (VTI) refrigeration device that allows temperature from  $\sim 1.4$  K to room temperature to be achieved. The VTI system is a vacuum sealed chamber in to which the sample probe is inserted and sealed at the top. This chamber is insulated from a bath of  $^4\text{He}$  in the main cryostat by a

**Table 3.1:** Operating the VTI under various temperature regimes.

Temperature range	Practice
1.4 K – 4.2 K	Fill VTI chamber with helium, close off needle valve and adjust the pumping rate to tune the temperature.
4.2 K – 300 K	Empty the VTI of helium and open the needle valve slightly, only pump a small amount and use the sample heater to set the temperature.

vacuum jacket.  $^4\text{He}$  is admitted into the VTI chamber from the bath via an adjustable needle valve and is pumped through the chamber and over the sample by an external roughing pump. By almost closing off the needle valve entirely and applying a heater on the sample stage the full range of temperatures can be achieved. In practice, a couple of temperature ranges are defined which require different operational techniques and are specified in table 3.1. The VTI chamber itself has an electric heater which can be operated separately and is good for rapidly heating the system up to room temperature but is in general too coarse for measurements.

Heating is controlled by a Lakeshore 340 temperature controller with the sample stage heated from the heater output and the VTI heater controlled from the analogue output which has been boosted via a custom built amplifier unit. Sample temperature is monitored by a Cernox mounted onto the sample stage and VTI temperature from a thermometer mounted inside the VTI chamber.

The sample stage can be rotated <sup>by</sup> ~~from~~ an external stepper motor which is supplied from a custom power source. All the instruments mentioned are controlled from a custom PC running a Delphi program written by Dr. M. French which queues runs, records and displays data. Some calculated values based on the raw data values are generated by the software, however these were not configured with the appropriate inputs. For this reason the angle and the current fields should be ignored and instead determined from raw data.

For twin voltage measurements, two Stanford SR830 lock-in amplifiers were used with one supplying the current and measuring voltage and the

second synchronised to the first and also measuring a voltage. The current supplied was supplied through a  $1\text{ k}\Omega$  buffer resistor in order to approximate the supply to a current source\*. The resulting voltages were passed through two passive Princeton Applied Research model 1900 low noise amplifiers set to  $\times 1000$  before measurement although the actual amplification for typical resistances of  $10\text{--}100\Omega$  at  $33\text{ Hz}$  is  $\times 980$ .

The sample probe has a rotating stage and so after aligning the sample roughly by eye, a shallow angle sweep in a low field, typically  $1\text{ T}$ , was performed before each measurement to make sure the sample was positioned perpendicular to the field. Some samples have an anisotropy in the transport terms and in the case of the Hall component, the effective field drops with the cosine of the angle of misalignment.

The magnet is superconducting and has a limit of  $14\text{ T}$  or  $16\text{ T}$  when using the additional cooling of the Lambda plate. For this thesis the measurements were only taken to  $13\text{ T}$  to minimise the risk of a quench. The field was ramped at  $1.4\text{ T/min}$ . The measurements presented in this thesis from the Polo magnet are all taken in the Hall configuration and are obtained by averaging both sets of contacts as described in the analysis section.

As of Feb 2012 it was determined using a Cu sample that a positive reading of the magnet power supply current (and field) corresponds to the magnetic field,  $B$ , in the Polo magnet pointing upwards. This was verified with a magnetic compass.

#### HFML Nijmegen

To access the normal state of the higher  $T_c$  materials we require fields larger than the  $13\text{ T}$  available in the Polo magnet at Bristol. The HFML facility in Nijmegen has available a continuous field Bitter magnet which can reach  $33\text{ T}$ . Data from Nijmegen in this thesis was taken in May 2010 by Dr. X. Xu, I. Mouzoupoulou, Dr. P. Rourke and Dr. A. McCollam.

The magnet used at the HFML sweeps at a rate of typically  $3\text{ T/min}$  meaning the temperature can drift significantly. The necessary heating supply for temperature control was alternated between a Lakeshore 340 temperature controller which uses input from a Cernox thermometer and a PID algorithm to supply an appropriate current or a Keithley current source

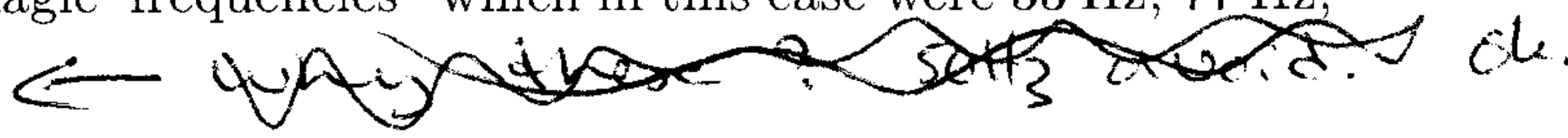
---

\*i.e. if  $(R_{\text{sample}} + R_{\text{wires}}) \ll R_{\text{buffer}}$  at all  $T$ , then the current is given by  $V_{\text{excitation}}/R_{\text{buffer}}$ .

*Depend on which way the leads are connected.*



which supplies a fixed current. The current source was selected on a sweep-by-sweep basis depending on which gave more stable temperatures. The analysis compensates for small drift using a simple correction described later.

The samples were measured using Stanford SR830 lock-in amplifiers which were supplying via  $1\text{ k}\Omega$  resistors with a  $10\text{ }\Omega$  shunt resistor. A  $1\text{ V}$  excitation voltage was used for all samples except for B00KOD1a and B16KOD1a where  $2\text{ V}$  excitation was used instead. The excitation frequency is set to one of the ‘magic’ frequencies\* which in this case were  $33\text{ Hz}$ ,  $77\text{ Hz}$ ,  $113\text{ Hz}$  and  $123\text{ Hz}$ .  ok.

Field is monitored using a calibrated Hall sensor mounted on the probe which is measured using another Stanford SR830 lock-in amplifier.

### LNCMI Toulouse

To obtain the highest fields we took measurements at the LNCMI pulsed field facility in Toulouse over the course of two separate visits. Here large capacitor banks are discharged through liquid nitrogen cooled copper resistive magnets to achieve short (few tens of microseconds) but strong fields of up to  $60\text{ T}$ . Pulses at the stronger end of the scale have more potential for damaging the magnet and take longer to cool down before the next pulse can be taken and so careful consideration is required to the magnitude of pulse undertaken. Typically the cooling time is around  $15$  to  $30$  minutes. The field is measured using a calibrated pick-up coil. The first trip took place in June 2009 and involved B. Arnold, Dr. P. Rourke, Dr. B. Vignolle and Prof. C. Proust. the second trip occurred in February 2010 and involved Dr. P. Rourke, Dr. J. F. Mercure, Prof. N. Hussey, Dr. B. Vignolle and Prof. C. Proust.

The results are recorded using a pair of Stanford SR830 lock-in amplifiers after passing through an active INA103 pre-amplifier set to a gain of  $\times 200$ . The raw signal for the pulse duration is recorded and the lock-in in algorithm is post-processed in software to avoid wasted pulses due to incorrect settings. The driving current is supplied by the lock-in amplifier and unless otherwise noted is  $5\text{ V}$  through a  $1\text{ k}\Omega$  resistor giving a current source of  $5\text{ mA}$ . The driving frequency is typically very high to sample the data over the relatively short pulse time and for these experiments is typically  $60\text{ kHz}$ . The data

---

\*Frequencies that do not fall near common sources of noise or their harmonics e.g.  $50\text{ Hz}$  from mains supply



is streamed via an optical link along glass fibres (so the chamber remain electrically isolated for safety during a pulse) to an external PC.

Cooling down to  $\sim 1.4$  K is possible by pumping on the helium in the magnet bath. Higher temperatures could be achieved by pumping out the exchange gas and heating via a Lakeshore 340 temperature controller. Although pulses are very short lived, there is a risk of the rapidly changing field inducing a current in the leads which cause heating of the sample during the pulse. For this reason great care is taken to minimise current loops by minimising the non-twisted portion of the wires leading to the sample. Furthermore, the sample is physically jolted by the high field which can adversely affect the data, for this reason, vacuum grease is carefully applied to the sample ensemble to reduce movement.

*more likely in the sample itself...*

For the first Toulouse visit, the measurements were taken in the magnetoresistance configuration, the second Toulouse visit measured the samples in the diagonal configuration.

### 3.4.2 Sample size determination

The length and the width of the samples were determined from calibrated optical microscope screen captures. The depth was determined post transport measurements with the help of Dr. P. Heard using a FIB. This images samples by rastering a focused beam of ions onto the sample surface and measuring the amount of ejected electrons or ions form the image. This process causes electrical charging of the surface which can in turn adversely affect the path of the highly focused incoming ions and so the sample to be imaged must be earthed in order to remain electrically neutral. For these samples, a line of 4929 silver paint was drawn between on of the contacts and the sample mounting puck.

### 3.4.3 Data Analysis

#### Isolating Hall and MR components

When measuring transport in a sample, there will always be contributions from both the MR and the Hall components due to imperfect geometry of the voltage pick up points. Since the Hall component reverses sign as the polarity of the field reverses whereas the MR component is independent of field polarity, the Hall and MR components can be separated out using the

following relations,

$$R_{\text{Hall}} = \frac{1}{2}(R_{\text{pos}} - R_{\text{neg}}) \quad (3.4.1)$$

$$R_{\text{MR}} = \frac{1}{2}(R_{\text{pos}} + R_{\text{neg}}) \quad (3.4.2)$$

where  $R_{\text{pos}}$  and  $R_{\text{neg}}$  are the resistances measured for the positive and negative field polarities. This requires data to be taken from the positive field maximum down to the negative field maximum and so for example with the Toulouse pulsed field apparatus, two pulses are required for each measurement.

### Analysis of the Hall angle

In metals the Hall component does not vary with temperature, however high- $T_c$  materials have consistently demonstrated a distinct non-trivial temperature dependence. One way to tackle this problem was pioneered by Chien *et al.* [74] who studied the Hall angle,  $\cot \theta_H = \rho(T)/(R_H(T)B)$ , of YBCO<sub>123</sub> doped with Zn impurities and found it to follow  $\cot \theta_H = aT^2 + C$  where  $C$  is a constant term due to impurities. The Hall angle,  $\tan^{-1}(\sigma_{xy}/\sigma_{xx})$ , is thought to cancel contributions from the transport scattering rate leaving the only the transverse scattering rate and so provides a way to access the 'actual' Hall contribution.

### Correcting for temperature variations

Figure 3.4.2 shows a comparison of typical field sweeps for the LNCMI and Nijmegen facilities and the Polo magnet. The LNCMI pulse length is  $\sim 150$  ms and as such is not typically subject to slow temperature drift throughout the duration of the pulse. However the positive and negative pulses are typically taken with at least a 30 min interval in-between pulses meaning the positive and negative pulses may not be at precisely the same temperature. As such, a small offset is applied to bring the zero field data into line between positive and negative pulses. For the longer sweeps such as the Nijmegen data sets, an additional offset was applied to the measurement which is proportional to the temperature as detailed below,

$$R_{\text{corr.}} = R_{\text{meas.}} + F(T_{\text{base}} - T_{\text{meas.}}) \quad (3.4.3)$$

not true: depends on the metal and the degree of  $T$  dependence.

better to delete this section

In free electron theory would be more accurate

but this does not explain why it is  $T$

dependent.

I don't see the relevance here of this

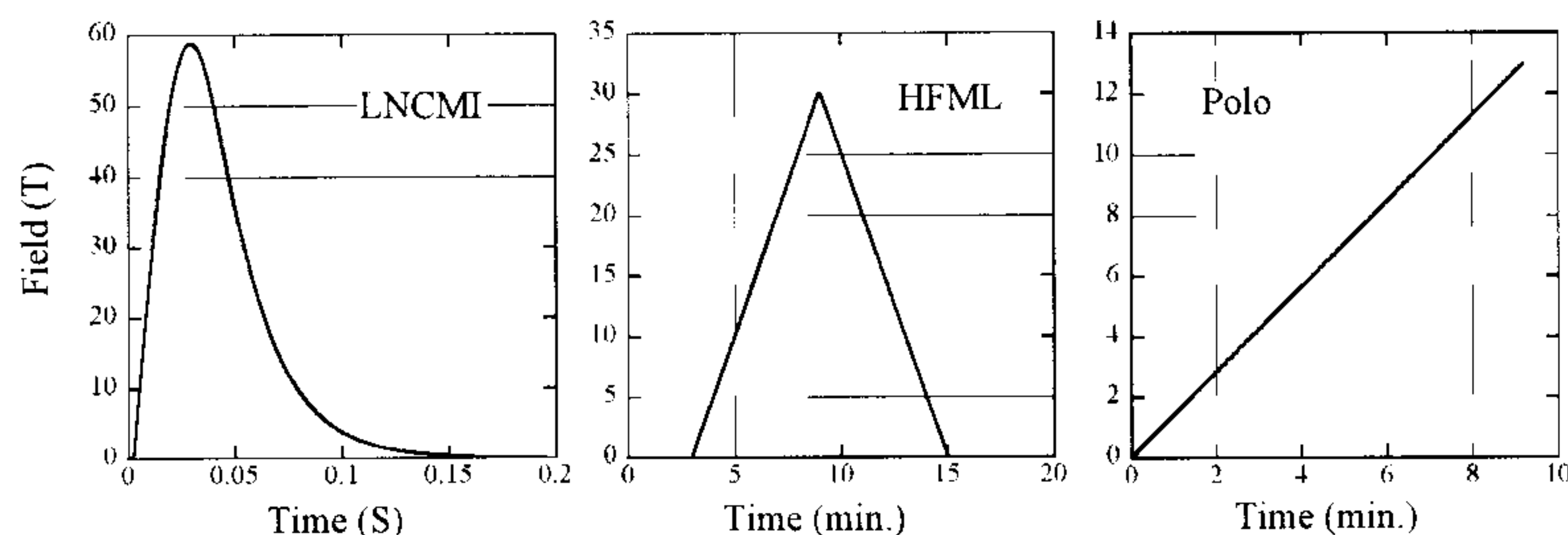


**Figure 3.4.2:** From left to right: Typical field sweep profiles for a pulse at the LNCMI, Toulouse, a continuous positive sweep at the HFML, Nijmegen and single positive upsweep for the Polo magnet, Bristol

where  $R_{\text{corr.}}$  is the corrected resistance,  $R_{\text{meas.}}$  is the measured resistance,  $T_{\text{base}}$  is the temperature that the resistance values are converged towards and  $F$  is an empirical scaling factor that brings the upsweep and downsweep data into line. The empirical factor was determined by inspection using the following method.

1. Take data where there is a clear component that is due to the temperature drift and find the appropriate factor so that it disappears. Take these data as reference benchmarks.
2. Where the temperature component is not so clear, use the reference data and make an informed estimate of the factor based on resistance vs. temperature curves in zero field and 13 T

The same factor is applied to both the positive and negative sweeps to avoid introducing artificialities into the Hall gradient. For the Polo data the temperature control was such that no correction was necessary.

### Field lag correction

The Polo magnet has no sensor to measure field at the sample, with the field values being calculated from the power supply current. In the data there is evident hysteresis in all sweeps and is illustrated in figure 3.4.3 which suggests that the actual field lags slightly behind the indicated field. To correct for this, the upsweeps and downsweeps were shifted towards each other until they overlapped, typically each by around 0.2 T. Any values which were corrected to less than 0 T or more than 13 T were then not used in the analysis.

*Why is this?*

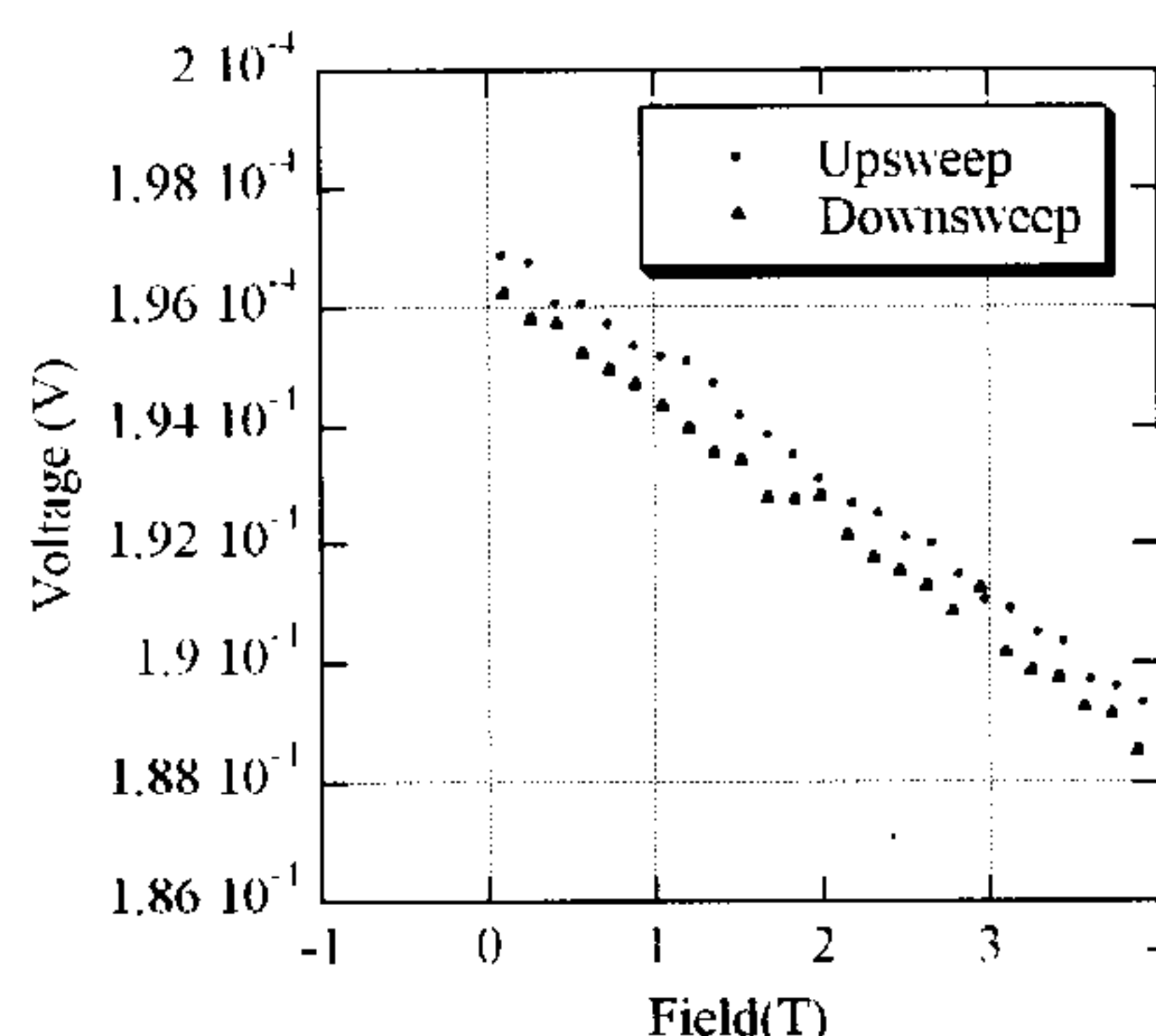


**Figure 3.4.3:** An example of the measured voltage of separate up and downsweeps which demonstrate the lag in actual field compared to the indicated field

### Combining up and downsweeps

For all the data values there is an upsweep portion and a downsweep portion which overlap and are averaged together to reduce noise. However many portions of data have regions which drift due to changes in the out-of-phase component or anomalies such as spikes and so in these cases the regions are recorded in a configuration file and the scripts that combine the sweeps ignore the problem regions and instead use data from the counterpart sweep in isolation. Similarly, when hysteresis is encountered in the pulsed data, by convention the upsweep is ignored since it tends to be more rapid than the downsweep which generally results in more spikes and out of phase problems.

it is more rapid.

To obtain the Hall and MR components using equation 3.4.1 we need to obtain comparable data points with shared field values. To do this one of two technique was employed. For the high-field data, this is done by binning the data and taking the average of the values in each of the bins so that they share the same field values. The data taken from the Polo magnet is linearly interpolated to a predefined set of field values.

### Linear fits to Hall data

Hall data for all samples were fitted using a standard linear least squares fit which was performed using Python for the Polo data and Delphi for the high-field data. A cutoff is specified so that only the data above the cutoff is fitted in the region where the linear behaviour is recovered. The cutoff value

why?  
the difference



is found by inspection of the Hall data with reference to the MR component. The precise point where linear behaviour is recovered is not always clear and so two cutoffs were specified which defined the upper and lower bounds for the start of the linear region. The limits contribute to the error in the Hall gradient with the final gradient being taken as the average of the fits from the two cutoff limits.

### Normalising the high field data

The Polo data was taken in the Hall configuration and so corresponds to the true Hall voltage, whereas the data from the first visit to the LNCMI was on sample measured in the MR configuration and so represent some unknown fraction of the true Hall voltage. Moreover, the rest of the high field data was taken in the diagonal configuration meaning the voltage path was over a different portion of the sample to the Hall measurement which again means the Hall voltage is scaled by some factor. For these reasons the Polo magnet measurements were taken as the canonical absolute values for the Hall data, with the high field data scaled so that concurrent data at higher fields aligned, this process along with the variation between fits using the two different cutoff bounds define the error bars in the data.

#### 3.4.4 Determining the doping

Three techniques have been identified for determining the doping for this thesis. The most simple and well known method for determining the doping of a material utilises the so-called ‘universal’ Tallon relation [75] which links  $T_c/T_c(\text{max})$  to  $p$  as follows,

$$T_c/T_c(\text{max}) = 1 - 8.26(p - 0.16)^2 \quad (3.4.4)$$

*error here*

This relation was established based on measurements of  $\text{La}_{2-x}\text{Sr}_x\text{CuO}_4$  (LSCO) which exploit the direct relation between Sr content and the doping (assuming stoichiometric oxygen).

The second technique, particular to  $\text{BSCO}_{2201}$ , was published by Ando *et al.* [10] in 2000 where samples of  $\text{BSCO}_{2201}$  were compared with Hall measurements of other cuprates where the carrier concentration is more easily determined, in particular LSCO was used again. The results lead to a very different relation between  $T_c/T_{c\text{max}}$  which confined superconducting

samples to a much narrower range of dopings\* and is given by the following relation,

$$T_c/T_c(\text{max}) = 1 - 254.3(p - 0.16)^2 \quad (3.4.5)$$

which was extracted from the Ando paper based on dopings determined by La concentrations.

There is however some doubt as to whether it is appropriate to compare LSCO and BSCO<sub>2201</sub> measurements across the superconducting dome, especially with regards to Hall measurements, given the proximity of the van-Hove singularity in LSCO which should lead to a depression in the apparent carrier density above  $p = 0.18$ .

The final technique is by comparing instead BSCO<sub>2201</sub> and Tl<sub>2201</sub> which have very similar structures, and van-Hove singularities at much higher doping than LSCO<sup>†</sup>. Doping in Tl<sub>2201</sub> has been well characterised in the overdoped side through recent dHvA experiments [77] which maps well to where the majority of our BSCO<sub>2201</sub> samples lie. Here the doping is determined using the Tallon relation for underdoped to slightly overdoped samples with  $T_c/T_c(\text{max})$  down to 0.71, below this value a linear relation is used:  $T_c/T_c(\text{max}) = 2.390 - 7.696p$ . Again some a priori knowledge of the approximate location (i.e. overdoped or underdoped) on the superconducting dome is required and further investigation may be required to determine which side of the dome a sample lies.

---

\*The justification being that increasing disorder suppressed  $T_c$  as you move away from optimal doping

<sup>†</sup>Tl<sub>2201</sub> has a van-Hove singularity at a much higher doping than even BSCO<sub>2201</sub>. At  $p = 0.26$  (or rather  $p = 1.26$ ), ARPES measurements have shown the van-Hove singularity in Tl<sub>2201</sub> lies a few eV below the Fermi energy [76]